Spatial–Temporal Soil Water Dynamics beneath a Tree Monitored by Tensiometer-Time Domain Reflectometry Probes

Sheng-Lun Li and Wei-Li Liang *

School of Forestry and Resource Conservation, National Taiwan University, Taipei 10617, Taiwan
* Correspondence: liangwl@ntu.edu.tw; Tel.: +886-2-3366-4616

Abstract: Tensiometer-coiled time domain reflectometry (T-TDR) probes have been developed in previous studies, but have not been applied in the field. In this study, we applied T-TDR probes to the simultaneous monitoring of soil water content (θ) and soil water potential (ψ) on a profile beneath a tree in a forest stand, and analyzed the temporal and spatial variations in soil water dynamics in a root-containing environment. The results showed different features in the relationships between the mean and standard deviation of spatial θ and ψ, which exhibited convex-upward shapes and negative curvilinear shapes, respectively. High spatial variability was observed at intermediate values of θ and small values of ψ. Matrix flow and preferential flow accounted for 75% and 25% of the area beneath the tree. Although the infiltration processes were dominated by matrix flow, preferential flow acting for a short time could cause an average θ or ψ to reach their maximum values at all of the locations. Preferential flow primarily occurred at a "hot spot" around a coarse root. Small changes in θ and ψ were generally observed at a "cold spot" beneath a lateral root. Integrated information from multiple sources of θ and ψ could help to evaluate soil water dynamics when one exhibited large spatial variation during the wetting or drying processes, and greatly help to improve the accuracy for detecting the presence of preferential flow in a short measurement period.

Keywords: matrix flow; preferential flow; TDR; tensiometer; tree root

1. Introduction

Soil water dynamics (e.g., the changes of soil water storage or movement) around a tree are highly variable, and are strongly affected by the spatial heterogeneity of water inputs through the canopy in the rainfall redistribution process [1–3], root-induced preferential pathways in the wetting process [4–6], and irregular drainage or water uptake by roots in the drying process [7,8]. Preferential pathways have often been identified using dye tracers and image analyses [9–11], data analyses of soil water responses [12,13], or both of tracers and field dataset [5]. The application of dye tracers could clearly visualize infiltration pathways and confirm the presence of preferential flow or matrix flow through the excavated soil profiles. The shortcoming of a dye experiment application is that the excavated soil profile for observing the dyed points is not available for soil water monitoring as it used to be. In addition to field observations, laboratory analyses of field soil samples are commonly used to determine soil hydraulic properties (e.g., water retention or permeability) or to estimate soil water behaviors (e.g., water storage or movement) in vegetation plots or forests [14–16]. However, many previous studies have indicated that soil water hydraulic properties or soil water behaviors determined using laboratory methods are not necessarily consistent with those observed in situ [17–20]. Although improved estimation methods for soil hydraulic properties are still needed, one of the most important applications of soil hydraulic characteristics is to estimate field soil water behaviors. In comparison to

dye experiments or laboratory analyses with field soil samples, using dataset (e.g., soil water content or potential) measured in fields to estimate soil water behaviors or to distinguish preferential flow or matrix flow is desired for the ongoing monitoring without destroying the observation profile.

Soil water storage and movement are mainly described by the changes of soil water content (θ) and soil water potential (ψ), respectively. Soil water sensors provide a direct method for monitoring soil water dynamics in the field using time-domain reflectometry (TDR) or capacitance and frequency sensors to measure θ [21,22], tensiometers to measure ψ [23,24], or combinations of these sensors [7,25]. Although measurements of both θ and ψ could comprehensively estimate field soil water dynamics, each of the sensors has been separately installed at the corresponded depths or locations so far, with the presumptively same volumes of the measured soil. Vaz et al. [26] argued that measurements of θ and ψ at different locations would make their interpretation difficult and uncertain. The interpretation would be more uncertain when θ and ψ are separately measured in the highly variable soil environments with tree roots and preferential pathways.

The development of multi-functional measurement sensors could greatly help by allowing the simultaneous acquisition of multiple data types at the same location, and by avoiding the potential error that results from separate measurements taken at different locations. For example, a combined penetrometer–moisture probe (CPMP) developed by Vaz and Hopmans [27] and improved by Kosugi et al. [28] can effectively provide simultaneous measurements of θ and soil resistance under both laboratory and field conditions. In CPMP sensors, the use and design of the coil-type TDR probe are important in relation to θ measurements. The coil-type TDR probe has been modified for sensor measurement techniques and used to measure water content in soil or bedrock environments [29–31], which may be employed for a variety of water content measurements by adjusting the probe size. Another application of the coil-type TDR probe, a tensiometer-coiled time domain reflectometry (T-TDR) probe, was previously developed in several sizes and designs [26,32,33]. Although simultaneous measurements of both θ and ψ are the greatest benefit of a T-TDR probe and the development and calibration procedures of the T-TDR probe have been conducted for many soil types [26,32], these tests and applications were only done under laboratory conditions. A T-TDR probe has not yet been utilized for monitoring soil water dynamics in the field in previous studies. Because controlled laboratory conditions and unexpected field conditions are different, it is still not clear whether the proposed designs of the T-TDR probes could be well applied in fields, particularly in soil environments that contain tree roots.

The main purpose of this study was to test the applicability of a T-TDR probe in a potentially heterogeneous soil environment with tree roots. Soil water dynamics underneath a tree were investigated using the modified T-TDR probes. Based on T-TDR models developed in previous studies, we modified the design of the T-TDR probe and enabled its application to field measurements. Using the dataset successfully recorded from 11 of these T-TDR probes during a short observation period of 1 month, we analyzed the soil water dynamics during the wetting and drying processes, and discussed the following issues:

1. Are the spatial variability of soil water described by θ and ψ different?
2. Could matrix flow and preferential flow underneath a tree be detected using the dataset of θ and ψ measured by the T-TDR probes in a short observation period?
3. What are the main effects of roots on soil water dynamics during the wetting and drying processes?

2. Materials and Methods

2.1. Design of a T-TDR Probe

Figure 1a shows the design of a custom-made T-TDR probe for use in the field, which was proposed in this study. For the TDR portion of the probe (Figure 1b), a pair of parallel tinned copper wires (diameter = 0.23 mm, length = 27.5 cm) was coiled at 5 mm intervals along a 62 mm long porous ceramic cup (diameter = 18 mm, wall thickness = 1.5 mm). The tinned copper wires were

bonded on the porous ceramic cup wall with epoxy adhesive (5 min AB adhesive; Araldite, Huntsman Corporation, Salt Lake City, UT, USA) (Figure 1c). The tinned copper wires were not completely covered by the epoxy adhesive, with glue applied only along two sides of the wires to maintain attachment between the tinned copper wires and the porous cup, and to reduce the influence of the epoxy adhesive on measurements. The tinned copper wires were connected to a coaxial cable and fixed using hot-melt adhesive (Figure 1b). The cable was guided along the outside wall of an L-shaped polyvinyl chloride (PVC) pipe, and connected to the TDR device of a TDR100 (Campbell Scientific, Logan, UT, USA) reflectometer through a coaxial multiplexer (SDMX50, Campbell Scientific). PC-TDR software (Campbell Scientific) was used for setup and waveform analysis. A pressure transducer (PA-750; Copal Electronics, Tokyo, Japan) was connected to the PVC pipe with a T-shaped PVC connector (Figure 1a). The pressure transducer records the gauge pressure at a resolution of 0.1% of the full scale (i.e., 1 cmH$_2$O), using a zero reference point of atmospheric pressure. We further modified the design of Vaz et al. [26] by reducing the diameter of the porous cup, which enabled easier field installation in areas with coarse roots or rocks. In the design reported by Vaz et al. [26], the 3 mm porous cup wall was machined to produce small grooves. The tinned copper wires were wrapped in these grooves to limit their movement during sensor installation. However, the machined grooves may damage the porous cup and affect the measurement of ψ. The machined grooves are also not suitable for small porous ceramic cups with thin cup walls. In our design, we carefully applied epoxy adhesive to fix the tinned copper wires to the outside of the porous cup instead of using machined grooves. The ratio of epoxy adhesive covered area to the total surface area of the porous cup was approximately 10% (Figure 1c), which would little influence the permeability of the porous cup. This avoided damaging the structure of the porous cup and reduced unexpected water leakage through the grooves.
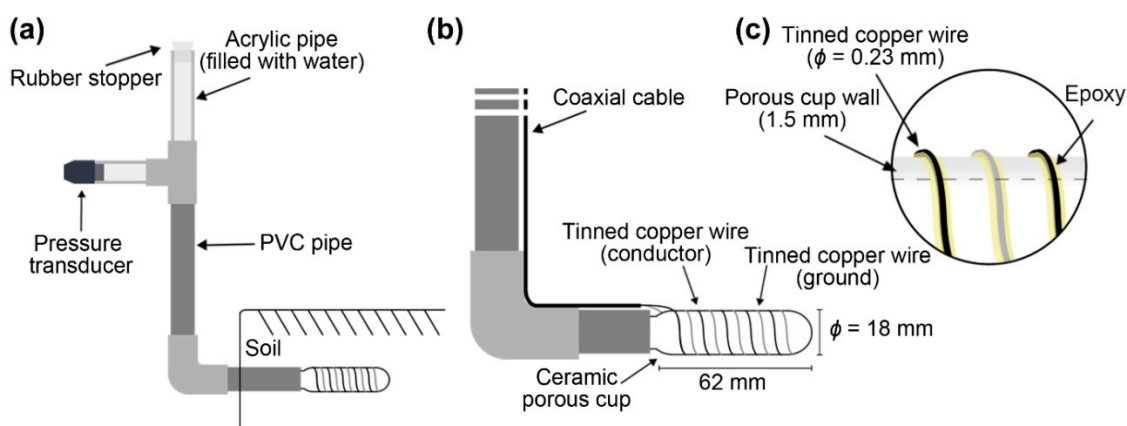

Figure 1. Design of the tensiometer-time domain reflectometry (T-TDR) probe showing (**a**) the side view inserted into the undistorbed soil profile, (**b**) the TDR portion of the probe, and (**c**) the portion of parallel tinned copper wires coiled along the porous ceramic cup.

2.2. Study Area and Sensor Installation

Observations were conducted for 1 month from 21 July to 26 August 2013 on a hillslope in the Neimaobu Tract of the Experimental Forest of National Taiwan University, central Taiwan (23°40′ N, 120°50′ E). The hillslope has a mean gradient of 15°, with clay loam soils underlain by sandstone and shale. The mean annual air temperature in 1990–2010 was 19.2 °C, with maximum and minimum monthly averages of 23 °C (July) and 14.2 °C (January), respectively. Mean annual precipitation was 2934 mm, with a wet season from May to August and a dry season from October to March. A Taiwania (*Taiwania cryptomerioides*) and Luanta-fir (*Cunninghamia lanceolata*) plantation, planted in 1984, were the predominant land covers. The plantation density was 2147 trees per ha with a spacing interval of approximately 2–3 m between trees [34]. Taiwania is a coniferous tree in the cypress family that is native to central Taiwan, and Luanta-fir is an endemic subspecies in Taiwan. Both tree species are

economically important in Taiwan. We selected a medium-size Taiwania tree with DBH (diameter at breast height) of 36.2 cm in the plantation, and dug a trench at a location 0.5 m from the tree with a depth of 90–100 cm and lateral length of 130 cm along the slope for observation of soil water dynamics (Figure 2a).
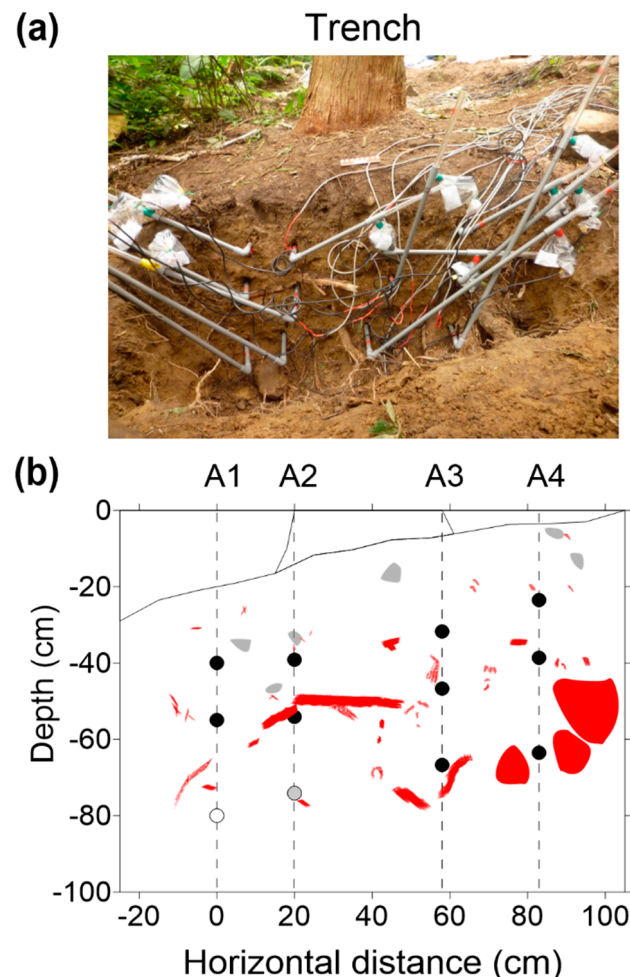

Figure 2. (**a**) Photographs and (**b**) sketches of the distribution of roots along the soil profile in the observation trench. In Figure 1b, A1–A4 indicate the vertical measurement lines, and grey and red shapes indicate the shape and size of rocks and roots observed in the profile exposed by the trench, respectively. Solid black circles indicate installation points of T-TDR probes that successfully monitored both soil water content and soil water potential during the observation period; a grey circle and an empty circle indicate points missing soil water content data, and missing both soil water content and soil water potential, respectively.

At the beginning of the experiment within 1 month before the observation period, 12 T-TDR probes were installed at three depths of 20 cm, 35 cm, and the trench bottom along four measurement lines (i.e., A1–A4) for simultaneous measurements of θ and ψ (Figure 2b). The bottom depths were 55 cm for A1–A3 and 60 cm for A4. We previously drilled holes (diameter = 15 mm, length = 10 cm) intersecting the soil profile at all installation locations, and carefully inserted all of the T-TDR probes into the holes (Figure 1a). It could get good contact with soils because the diameter of the hole was smaller than that of the T-TDR probe. Then, the trench was backfilled with field soils without rocks and stood for a month to stabilize the backfilled soils. During the observation period, however, θ and ψ at 60 cm in A1 and θ at 55 cm in A2 had missing measurement values due to the loose of copper wires and damage of a porous cup at the time of installation. Thus, θ was recorded at 10 points (black

circles in Figure 2b) and ψ recorded at 11 points (black and grey circles in Figure 2b) for analysis in this study. Before backfilling the trench, we observed and sketched the distributions of rocks and roots exposed on the soil profile (Figure 2b). A coarse root (10–20 cm in diameter) intersected the soil profile at a depth of 60 cm around measurement line A4, and a lateral root (3 cm in diameter) ran parallel to the soil profile a depth of 35 cm between measurement lines A2 and A3. Some rocks and fine roots were also found throughout the soil profile, but roots were sparse below a depth of 60 cm, which was near the soil–bedrock interface. All of the devices at the observation site were connected to a data logger (CR1000; Campbell Scientific), which recorded observations at 10 min intervals. Open-area rainfall measured at a location (23°41′ N, 120°57′ E) 16.6 km from the observation site was used.

2.3. Calibration of the T-TDR Probes

After the observation period, all of the T-TDR probes installed at the site were removed. Then, 6 of the 12 T-TDR probes were used for laboratory calibration with reference to the θ values derived from three commercially supplied and calibrated θ sensors (EC-5; Decagon Devices, Pullman, WA, USA; see Figure S1a and Table S1 in Supplementary Materials). Due to the interruption of roots, it was hard to sufficiently sample the soils around the T-TDR probes. Instead, the field soils used for investigating general properties and calibrating the T-TDR probes were sampled at a location with few rocks and roots, 3 m from the observation tree. The general properties of the field soil (Table 1) were investigated using undisturbed soil samples, which were taken from three depths (i.e., 20, 35, and 60 cm) using thin-walled steel samplers with a volume of 100 cm^3 per sample. The physical properties and textures of the field soils at these three depths were very similar (Table 1), and all of them were classified as clay loam based on the United States Department of Agriculture soil texture triangle. Calibrations were conducted using disturbed field soil samples which were separated in to three groups with three different particle size distributions. They were the mixed soils sampled at three depths (i.e., clay loam), the mixed soils retained by a soil sieve with 2-mm openings (denoted "coarse loam"), and the mixed soils passing through a soil sieve with 2-mm openings (denoted "fine loam").

Table 1. Physical properties of field soils at different depths based on three undisturbed samples collected at each depth.

Depth (cm)	Particle Density (g/cm^{-3})	Bulk Density (g/cm^{-3})	Porosity (%)	Sand (%)	Silt (%)	Clay (%)
20	2.18	1.32	39.6	33.8	35.6	30.6
35	2.27	1.46	35.8	36.3	34.4	29.4
60	2.23	1.40	37.4	34.1	33.2	32.7

As detailed in Supplementary Materials, the measured dielectric constant (ε) was calibrated to θ using a third-order polynomial regression equation for each soil (see Figure S3 and Table S2). The performance of the calibrated T-TDR probes was equivalent to EC-5 sensors, with an accuracy of ±0.033 cm^3/cm^3 to measure θ (see Figure S4 and Table S3). To verify which calibration equation was appropriate, we compared the ψ and ε obtained from the backfilled trench during the observation period to those measured in the calibration procedure, and found that the shape of the ε-ψ curve for coarse loam most closely matched the ε-ψ curve for the backfilled trench (see Figure S5). Thus, the calibration equation for coarse loam (see Table S2) was used to convert the output values of ε from the T-TDR probes to θ for the field observations.

2.4. Data Analyses for Soil Water Dynamics

Using the θ and ψ dataset measured using T-TDR probes during the observation period, we analyzed (1) the temporal variation in θ and ψ, and the spatial variation in soil water dynamics (2) during rainfall events and (3) during a dry period, corresponding to three issues discussed in

this study. For the analysis (1), the relationships of the mean (μ) and standard deviation (σ) of θ and ψ at each depth during effective rainfall events and outside of such events were analyzed separately. Each individual rainfall event was separated from other events by 6 consecutive hours without rainfall. This criterion corresponds to previous studies focused on hydrological responses in shallow soil layers [21,35,36]. An effective rainfall event was defined as the event that resulted in significant hydrological responses in θ and ψ. The significant hydrological responses were defined as the increases of average θ and ψ at all of the measurement points of more than 0.005 cm^3/cm^3 and 5 cmH_2O, respectively.

For the analysis (2), the detailed spatial variations in θ, ψ, and hydraulic potential (φ) in the soil profile were investigated for the two largest events in the observation period. The φ value was computed as the sum of the ψ value and the height (z) at which ψ measured (i.e., φ = ψ + z). Flux vectors were determined based on the 11 measurement points of φ which were interpolated using the ordinary Kriging method with a simple linear model (Surfer ver. 13; Golden Software, Golden, CO, USA). In addition, the general patterns of soil water dynamics in space were investigated for all effective rainfall events. Lozano-Parra et al. [13] assumed that slow and rapid responses of soil water are caused by matrix flow and preferential flow, respectively, and used the maximum slope of the wetting curve (i.e., the time derivative of soil water increase) during rainfall events to determine whether the hydrological response was dominated by matrix flow or preferential flow in several plots within a catchment. As similar ideas of Lozano-Parra et al. [13], we identified the maximum increases of θ ($\Delta\theta_{max}$) and ψ ($\Delta\psi_{max}$) with a 10 min measurement interval at each point during effective rainfall events using Equations (1) and (2):

$$\Delta\theta_{max,i} = Max\ (\theta_i^{t+1} - \theta_i^{t}) \tag{1}$$

$$\Delta\psi_{max,i} = Max\ (\psi_i^{t+1} - \psi_i^{t}) \tag{2}$$

where i represents each measurement point (i = 1–10 for θ_i; i = 1–11 for ψ_i), and t + 1 and t are time steps at 10 min measurement intervals. Because $\Delta\theta_{max}$ or $\Delta\psi_{max}$ among measurement points were not necessarily detected at the same time during an event, $\Delta\theta_{max}$ or $\Delta\psi_{max}$ was compared to the average rainfall intensity by dividing the accumulated rainfall amount by the duration from the start of a rainfall event to the time that $\Delta\theta_{max}$ or $\Delta\psi_{max}$ was reached. Moreover, water storage and saturation generation capabilities were analyzed at each point. The increase in θ at each point (S_i) was quantified from the start of an event ($\theta_i^{initail}$) to the time at which average θ for all of the measurement points reached its maximum value (θ_i^{max}) during each effective rainfall event, (i.e., $S_i = \theta_i^{max} - \theta_i^{initail}$). Then the standard score (Z-score) was used to remove the rainfall magnitude factor, and the normalized index of S_i^{*} was rescaled by:

$$S_i^* = (S_i - \mu)/\sigma \tag{3}$$

where μ and σ are the mean and standard deviation of S_i at all points (i = 1–10) for an event, respectively. Thus, S* could represent where water was generally stored at the wettest time (i.e., the maximum value of the average θ at all measurement points) in an event, which is different to $\Delta\theta_{max}$ that might be not necessarily detected at the same time among measurement points. Similarly, the duration of saturation occurrence (i.e., ψ = 0 cmH_2O) at each point (D_i) was investigated from the start to the end of each effective rainfall event. Then the normalized index of D_i^{*} was rescaled using the standard score:

$$D_i^* = (D_i - \mu)/\sigma \tag{4}$$

where μ and σ are the mean and standard deviation of D_i at all points (i = 1–11) for an event, respectively. Thus, D* represents the point where saturation generally occurred and remained during an event.

For the analysis (3), the detailed spatial variations in θ, ψ, and φ in the soil profile were investigated during the drying period from 31 July to 15 August 2013 (Figure 3). The drying period persisted for approximately 14 days without effective rainfall events. The instantaneous rates of θ and ψ depletion

(i.e., depletion amount/time interval) at each measurement point were calculated during the drying period. In this calculation, the variable time interval (Δt) was defined as the interval with a decrease in θ or ψ at each point of more than 0.001 cm^3/cm^3 or 15 cmH$_2$O, respectively. Because the instantaneous depletion rate is controlled by the value of θ or ψ, the instantaneous depletion rate was compared to the average θ or ψ between the start and end of Δt.
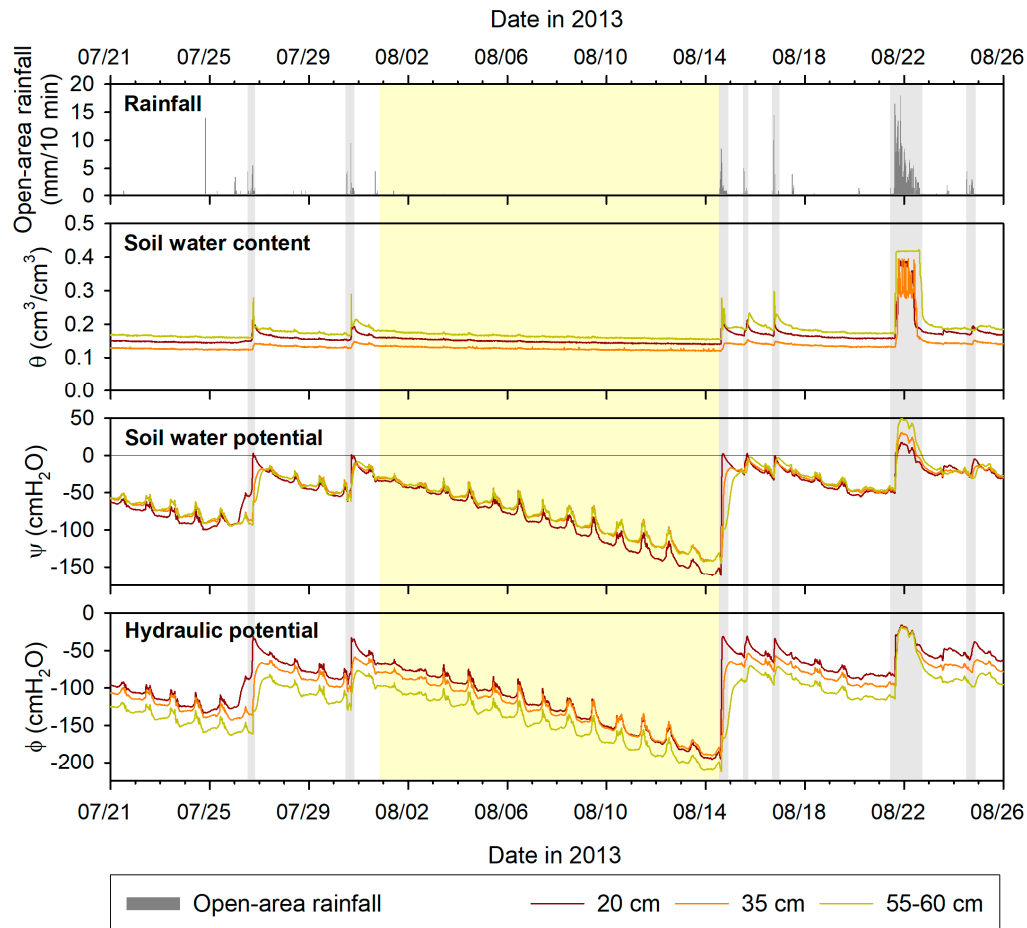
Figure 3. Temporal variation in open-area rainfall, and the average values of soil water content (θ), soil water potential (ψ), and hydraulic potential (ϕ) at each observation depth during the entire observation period. The yellow and grey shaded intervals correspond to a drying period and the effective rainfall events, respectively.

3. Results

3.1. Temporal Variation in Soil Water Dynamics

There were approximately 24 rainfall events recorded during the observation period, in which significant hydrological responses were detected for the 7 effective rainfall events with total rainfall amounts of 23.0–637.0 mm (Figure 3 and Table 2). The θ and ψ at three depths increased rapidly during the effective rainfall events and decreased gradually during periods without rainfall (Figure 3). In the periods without rainfall, the decreases were small in θ but relatively large in ψ. This was attributed to characteristics of soil water retention that θ varies little in the high-suction region (see Figure S8). The diurnal vibration observed in ψ and ϕ, particularly in periods without rainfall, were likely due to the temperature of the pressure transducer increasing in direct sunlight. During the effective rainfall events, positive ψ and generation of transient saturation were observed at some depths. The ϕ value was generally greater at shallow depths during the observation period, except during the latter half of the drying period and the largest event, in which ϕ at deeper points was greater or equal to that

at shallower points. This indicates that downward vertical movement of soil water fluxes generally occurred in the study area.

Table 2. Properties of the effective rainfall events.

Event	Start	End	Duration (hr)	Total Rainfall (mm)	Max. Rainfall Intensity (mm/10 min)
1	26 July 2013 12:30	26 July 2013 19:40	7.2	40.0	5.5
2	30 July 2013 12:30	30 July 2013 20:20	7.8	40.5	9.5
3	14 August 2013 13:10	14 August 2013 21:50	8.7	75.0	8.5
4	15 August 2013 12:30	15 August 2013 17:00	4.5	23.0	5.0
5	16 August 2013 16:10	16 August 2013 22:30	6.3	45.0	14.5
6	21 August 2013 10:30	22 August 2013 17:50	31.3	637.0	18.0
7	24 August 2013 12:10	24 August 2013 20:10	8.0	40.0	4.5

It should be noted that θ vibrated greatly at 20 cm and 35 cm during the largest event when large positive values of ψ were recorded, which did not occur during the other rainfall events (Figure 3). This finding was attributed to the waveform length parameter setting applied in the TDR waveform analysis software PC-TDR, which must be large enough to extend a short distance past the end of the probe under the wettest expected conditions [37]. Although the waveform length that we employed (i.e., 4 m) was recommended by Campbell [37], the wettest condition exceeded our predictions. We infer that the vibrations in θ would plateau and maintain high values if a larger waveform length had been set. As reference data, ψ at depths of 5–65 cm were measured with the calibrated EC-5 sensors in another trench adjacent to the main trench in the present study (see Figure S2). Temporal variations in ψ measured by the T-TDR probes and EC-5 sensors were reasonably well matched in both rainfall and no-rainfall periods (see Figure S6). Particularly, ψ measured by both the T-TDR probes and EC-5 sensors plateaued at high values during the largest event when soil became saturated, and decreased gently during the no-rainfall periods. It suggested that the performance of the calibrated T-TDR probes in the field was equivalent to that of EC-5 sensors.

During the observation period, the relationships of the mean and standard deviation in θ and ψ differed between the periods in the effective rainfall events and outside of the events. For θ during the effective rainfall events (Figure 4a), both the mean and standard deviation varied greatly, and their relationship showed a convex-upward shape at all three depths. In the early stage in the effective rainfall events, the standard deviation increased with small values of the mean, reached a maximum at intermediate mean values, and decreased at the larger mean values. In the late stage in the events, when the mean decreased, the relationship between the mean and standard deviation also exhibited convex-upward shapes but shifted in the opposite direction. For θ in the periods outside of the events (Figure 4b), both the mean and standard deviation were small during drying processes, and the standard deviation generally decreased with decreasing mean at each of the three depths. For ψ during the effective rainfall events (Figure 4c), the standard deviation decreased with increasing mean values, and plateaued approximately when ψ became positive at each depth. In the late stage in the events, when the mean decreased, the standard deviation increased along with the decreasing mean. For ψ in the periods outside of the events (Figure 4d), the standard deviation increased as the mean decreased, exhibiting negative curvilinear shapes during the drying processes. It is notable that ψ at depths of 35 cm and 55–60 cm showed obvious hysteresis, with larger standard deviation at relatively

high mean values. This type of hysteresis only occurred for events that started with dry soil conditions and had low rainfall supply (i.e., the events ending on 26 July and 14 August, shown in Figure 3). Thus, the dry conditions remaining in deeper layers after these events led to higher standard deviation of ψ.
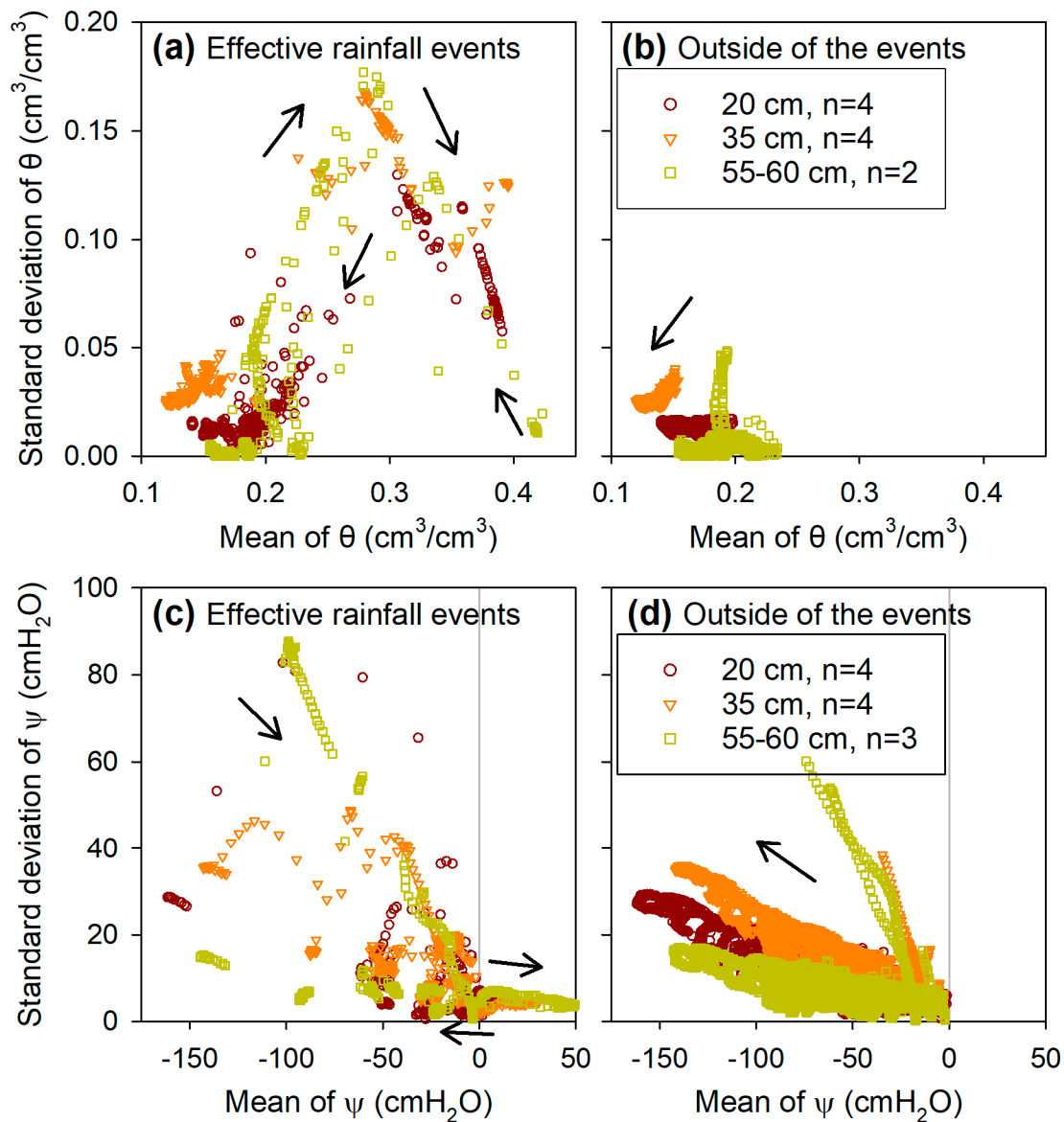

Figure 4. Relationships between the mean and standard deviation (denoted "μ-σ") of soil water content (θ) during (**a**) the effective rainfall events and (**b**) outside of the events, and the μ-σ of soil water potential (ψ) during (**c**) the effective rainfall events and (**d**) outside of the events. The n indicates the sample size of soil water content or soil water potential used for deriving the μ-σ at each depth. Arrows indicate transition dynamics.

3.2. Spatial Variation in Soil Water Dynamics during Rainfall Events

Figure 5 shows the spatial distributions of θ, ψ, and soil water flux vectors in the soil profile during the second largest event of the observation period. The event on 14 August can be characterized as an afternoon shower with total rainfall of 75 mm. At the start of the event (i.e., T0), the soil profile was in a relatively dry condition, with average θ and ψ of 0.14 and −139 cmH$_2$O, respectively. The flux vectors were irregular, with upward, lateral, and downward directions. At 140 min after the peak of rainfall (i.e., T1), θ and ψ generally increased with increasing depth, except for the point at 60 cm

depth in A4, where a coarse root intersected the soil profile and greater increases of both θ and ψ were recorded. The flux directions were generally downward, except for the deeper layer around A1 and A4 where obvious lateral fluxes were observed. At 260 min, when rainfall intensity weakened (i.e., T2), the spatial distributions of θ and the flux vectors changed little in comparison to those at T1, but ψ remained to increase from shallow to deep layers. At the end of the event (i.e., T3; 520 min), θ gently decreased at most points, while ψ and the magnitude of the flux vectors continued to increase in the deeper layers.
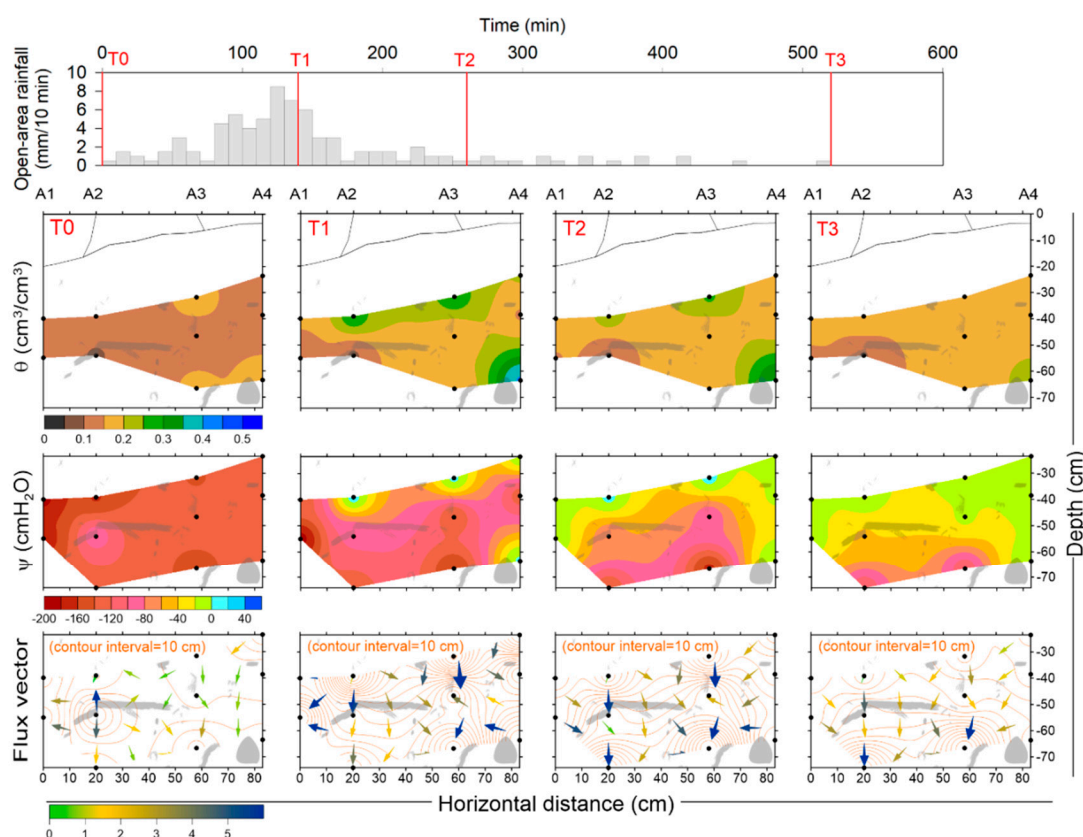
Figure 5. Spatial distributions of soil water content (θ), soil water potential (ψ), and flux vectors (from top to bottom rows) after 0 (T0), 140 (T1), 260 (T2), and 520 (T3) min (from left to right columns) during the second-largest rainfall event in the observation period. The size and direction of arrows indicate flux vectors (cmH$_2$O/cm), which are plotted based on the spatial distribution of the hydraulic potential, which is shown with contour lines. Black circles and gray shapes on each plot indicate measurement points and roots exposed in the soil profile, respectively.

Figure 6 shows the soil water dynamics during the largest event of the observation period. The event on 21–22 August was caused by a typhoon, with total rainfall of 637.0 mm, respectively. At the start of the event (i.e., T0), the soil profile was in a relatively wet state, with average θ and ψ of 0.15 and −44 cmH$_2$O, respectively. The flux vectors were small and generally directed downward. At 330 min, when accumulated rainfall was 69.5 mm (i.e., T1), both θ and ψ increased markedly at all depths in A1–A4, except for the area underneath lateral roots that run parallel to the soil profile. Significant increases in θ, ψ, and lateral fluxes were found at a depth of 60 cm in A4, as similar as those shown at T1 in Figure 5. At 690 min, after the continuous high rainfall intensities (i.e., T2), great increases in θ were observed at all points, and ψ became positive at all of the points. Both the mean of θ and the mean of ψ at all of the points reached their maximum for this event. The magnitude of the flux vectors became small, and most of their directions changed from downward to lateral or upward, as all of the points were saturated. At 1730 min, around the end of the storm event (i.e., T3), large θ

and positive ψ were only observed at points deeper than 50 cm. The lateral flux vectors returned to a downward-dominant pattern, similar to those at T0. The observations during the two largest events suggest soil water dynamics were primarily controlled by the slow movement of the wetting front at lines A1–A3, but featured rapid, large responses of θ and ψ in deeper layers of A4, even when the accumulated rainfall was low (e.g., at T1 shown in Figures 5 and 6).
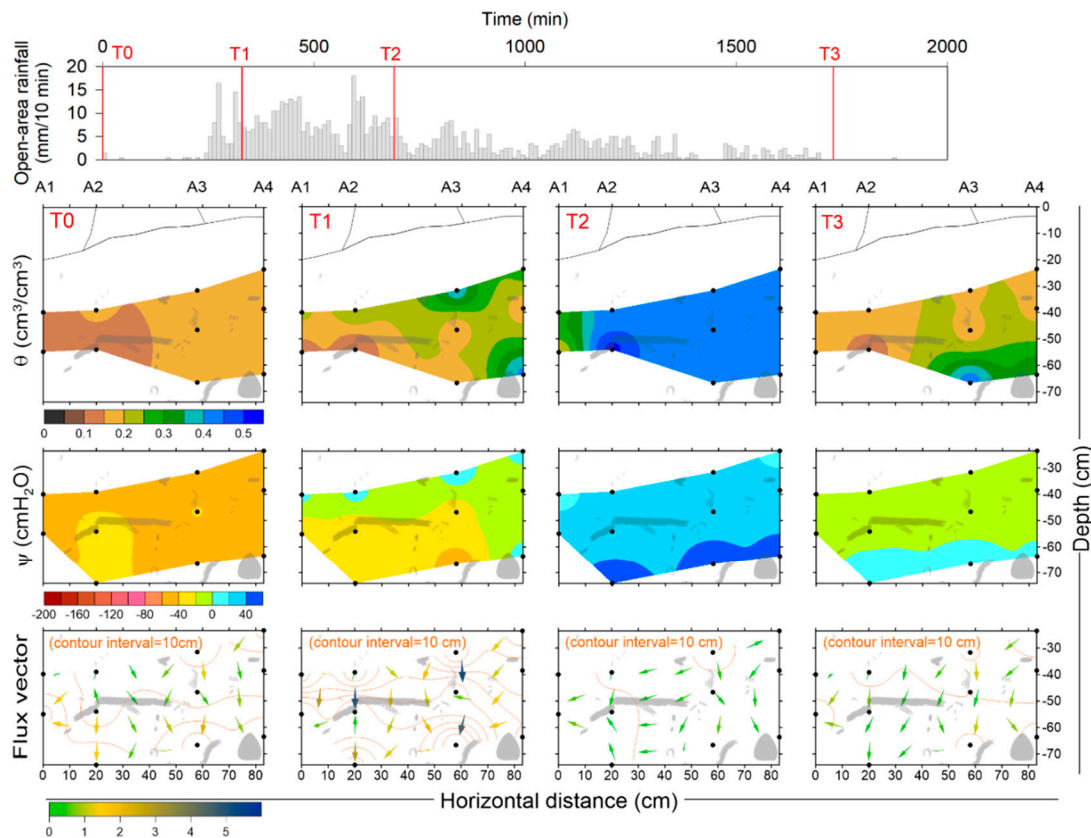

Figure 6. Spatial distributions of soil water content (θ), soil water potential (ψ), and flux vectors after 0 (T0), 330 (T1), 690 (T2), and 1730 (T3) min during the largest rainfall event in the observation period. Other details are as described for Figure 5.

In addition to the detailed soil water dynamics observed during the two largest events, we also analyzed the general patterns of the hydrological responses at each point for the seven effective rainfall events. Figure 7 presents the relationships of $\Delta\theta_{max}$ and $\Delta\psi_{max}$ to the average rainfall intensity whenever $\Delta\theta_{max}$ and $\Delta\psi_{max}$ were recorded during an event. Assuming a slowly progressing wetting front, $\Delta\theta_{max}$ and $\Delta\psi_{max}$ can be expected to be greater at shallower depths. The expected pattern was observed in A1–A3, but did not match to the field response measured in A4, where $\Delta\theta_{max}$ and $\Delta\psi_{max}$ were greater at the 60 cm depth. This finding suggests that the general patterns of the hydrological responses at A1–A3 and A4 are dominated by matrix flow and preferential flow, respectively. Because the results in Figure 7 would be affected by initial soil conditions and rainfall characteristics, we further tested whether the response patterns differed between A1–A3 and A4 (Figure 8). The rescaled S* and D* values were used to evaluate the capabilities for soil water storage and saturation generation, according to Equations (3) and (4). Both S* and D* were greater at 20 cm than at 35 cm or 55–60 cm depths in A1–A3, and most observations at 20 cm were greater than the average value of all points (i.e., S* and D* = 0). However, S* and D* in A4 showed greater values at deeper points, which were even greater than the mean value of all points. Based on the arithmetic mean, the maximum S* and D* values were observed in A4 (i.e., 0.59 and 0.19), and the minimum S* and D* values occurred in A1 (i.e., −0.41 and −0.42), among the four measurement lines. The soil water responses shown in Figures 7

and [8] demonstrated a depth-dependent pattern in A1–A3 and a depth-independent pattern in A4, even though the physical properties and textures of the field soils were similar at three depths (Table 1). The depth-dependent and depth-independent patterns were likely dominated by matrix flow and preferential flow, respectively.
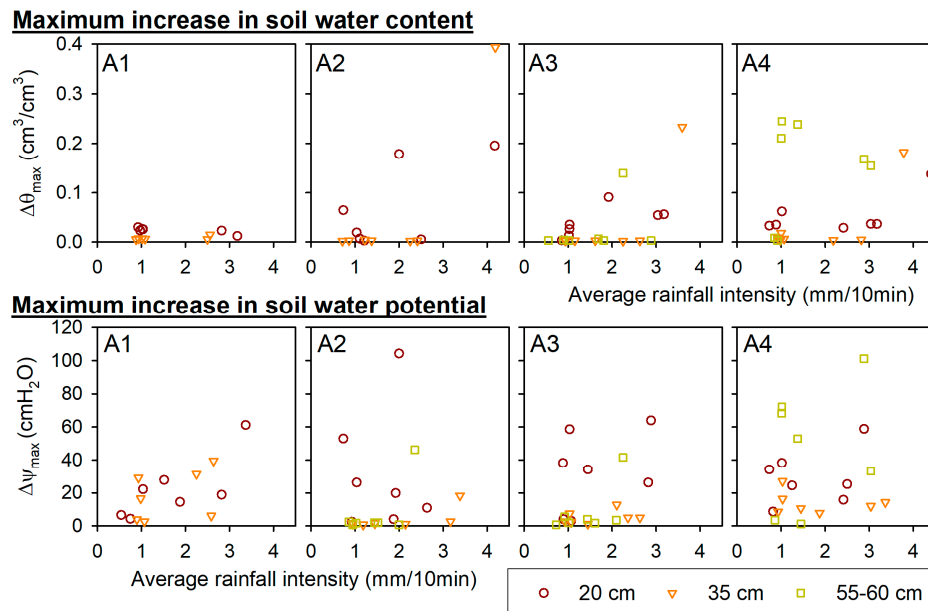

Figure 7. Relationship of the maximum increase in soil water content ($\Delta\theta_{max}$) and soil water potential ($\Delta\psi_{max}$) at each point on measurement lines A1–A4 to the average rainfall intensity when $\Delta\theta_{max}$ or $\Delta\psi_{max}$ was reached at a 10 min measurement interval during the effective rainfall events.
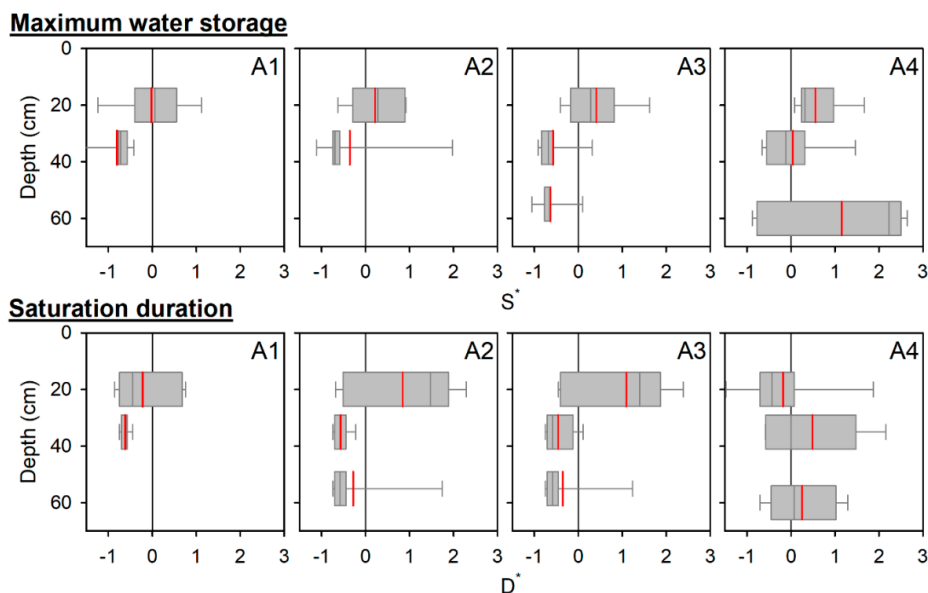
Figure 8. Variation in rescaled water storage (S*) and rescaled saturation duration (D*) at each point on measurement lines A1–A4 during effective rainfall events. Boundaries of the box indicate the 25th and 75th percentiles, the grey line within the box shows the median value, the red line indicates the mean value, and error bars represent the 10th and 90th percentiles.

3.3. Spatial Variation in Soil Water Depletion during a Drying Period

Figure 9 shows the spatial distributions of θ, ψ, and soil water flux vectors at four time points measured at 12:00 p.m. on various days (i.e., at 0.7, 4.7, 8.7, and 13.7 days post-rainfall) during

the drying period. Although θ and ψ at all of the points decreased with the duration of drying, and this depletion seemed to expand from the downslope to upslope sites (i.e., from A1 to A4); the depletion was not depth-dependent. This result was inconsistent with general understanding of greater depletion at shallower depths due to evaporation. The directions of the flux vectors shifted from a downward-dominant pattern to irregular, and the magnitude of the flux vectors increased at specific points as the drying duration increased, particularly at the 35 cm depth of A2, beneath the lateral root. The instantaneous depletion rates of θ decreased with decreasing θ values at all of the points, in which the depletion rate decline was location-dependent and differed by several orders of magnitude (Figure 10). Based on the geometric mean, the maximum and minimum instantaneous depletion rates of θ occurred at the 35 cm depth of A1 (4.08×10^{-3} cm^3/cm^3/day) and the 35 cm depth of A4 (1.49×10^{-3} cm^3/cm^3/day) among all of the points, and in A1 (3.39×10^{-3} cm^3/cm^3/day) and A4 (2.42×10^{-3} cm^3/cm^3/day) among the four measurement lines. Unlike θ, most of the instantaneous depletion rates of ψ increased with decreasing ψ values, and the rates at some points varied little with ψ values (Figure 10). Based on the arithmetic mean, the maximum and minimum instantaneous depletion rates of ψ were observed at 35 cm depth in A1 (12.5 cmH$_2$O/day) and 35 cm depth in A2 (5.4 cmH$_2$O/day) among all of the points, and in A1 (11.9 cmH$_2$O/day) and A4 (8.4 cmH$_2$O/day) among the four measurement lines. The results described above indicate that the depletion of θ and ψ did not depend on depth, but expanded from downslope to upslope points. However, the depletion rates were location-dependent. In particular, the instantaneous depletion rates of ψ at the 35 cm depth in A2 were very small, which resulted in relatively high values of ψ during the late stage of the drying period, and caused upward, lateral, and downward flux vectors with large values at this location (Figure 9).
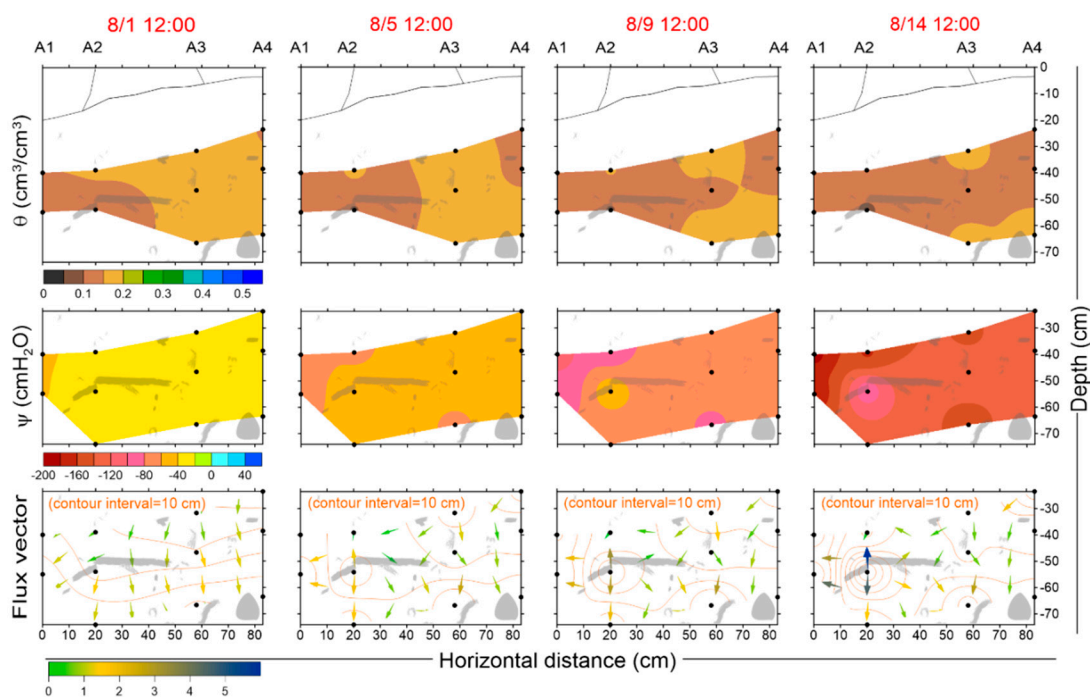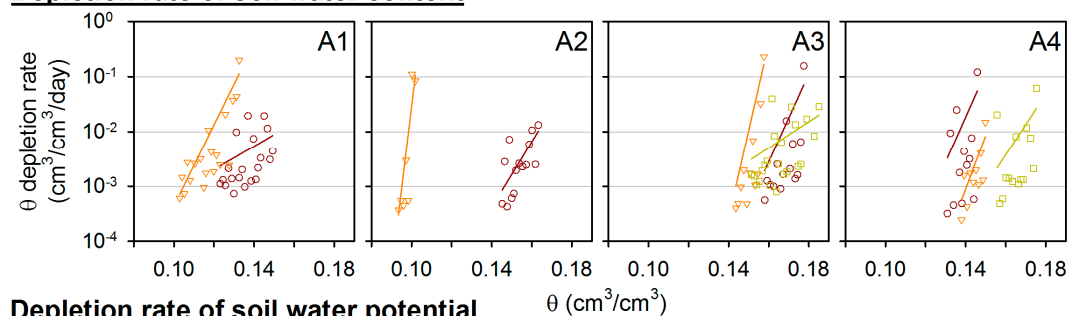

Figure 9. Spatial distributions of soil water content (θ), soil water potential (ψ), and flux vectors at four time points during the drying period from 31 July to 15 August 2013. Other details are as described for Figure 5.
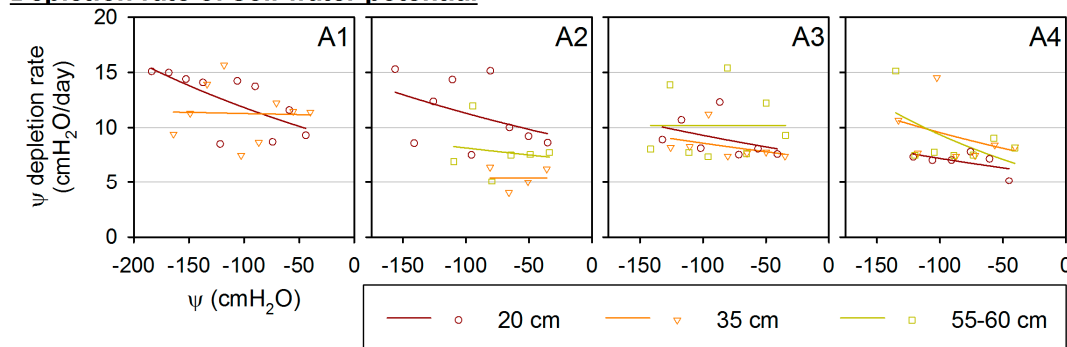
Figure 10. Instantaneous depletion rates of soil water content (θ) and soil water potential (ψ) against the values of θ and ψ at each point on measurement lines A1–A4 during the drying period from 31 July to 15 August 2013. An exponential trend line is fitted to the data at each measurement depth.

4. Discussion

4.1. Relationships between the Mean and Standard Deviation of Soil Water Content and Soil Water Potential

The relationship between the mean and standard deviation (denoted "μ-σ") of spatial θ or ψ values was used to evaluate the hydrological behaviors in several environments. The μ-σ of θ had positive curvilinear shapes [38,39], negative curvilinear shapes [40,41], and convex-upward shapes [42,43]. The μ-σ with convex-upward shapes and variance peaks at intermediate values of θ is the representative pattern [44], which has also been observed for a range of land uses and across the scales of the hillslope, catchment, and region [45–47]. Compared to θ, the μ-σ of ψ is relatively simple, although it has been less frequently reported. In early studies using tensiometers in the field, Greminger et al. [48] and Yeh et al. [49] presented a dataset showing that the standard deviation increased with decreasing mean ψ. In recent studies, the μ-σ of ψ with negative curvilinear shapes were observed at the depths of 10–100 cm [50] or at the soil–bedrock interface [51]. Base on the previous studies above, the μ-σ of spatial θ with convex-upward shapes and the μ-σ of spatial ψ with negative curvilinear shapes are recognized the representative patterns. It suggests that different spatial variations in hydrological behaviors described by θ and ψ.

At our study site, the representative patterns of the μ-σ of both θ and ψ were observed using T-TDR probes in a short observation period (i.e., 1 month) that included large rainfall events and a 2-week drying period. The μ-σ of θ (Figure 4a) exhibited convex-upward shapes at all three depths, consisting of positive curvilinear shapes in the drying processes and negative curvilinear shapes at the high values of θ during the wetting processes. The μ-σ of ψ (Figure 4d) had negative curvilinear shapes at all three depths. The spatial variation (i.e., the standard deviation) reached its maximum values at intermediate mean values of θ, but increased with decreasing mean ψ. This indicates that the specific ranges of θ and ψ that exhibit large spatial variation required higher measurement resolutions, and also suggests the advantages of θ sensors for measurement under relatively wet conditions and of ψ sensors for measurements under relatively dry conditions. For the study issue 1, therefore, T-TDR probes can simultaneously capture the different characteristics of both θ and ψ during the wetting or

drying processes, even when used for a short observation period. Moreover, integrated information from multiple sources of θ and ψ could help to evaluate soil water dynamics when one exhibited large spatial variation during the wetting or drying processes.

4.2. Effects of Roots on Soil Water Dynamics underneath the Tree

As noted by Ghestem et al. [52], preferential flow occurs in channels formed by dead or decayed roots and around live roots. The preferential pathway formed by tree roots is wider and deeper than those of crops or pasture plants [53], and is the normal phenomenon rather than an exception in the field [54]. Using a similar analysis method as this study (Equation (1)), however, Lozano-Parra et al. [13] quantified matrix flow as a general pattern of soil water dynamics that occurred more frequently (>50%) than preferential flow (<30%) among several plots in a catchment in Spain. Lin and Zhou [12] also reported a small amount of preferential flow with an overall average frequency of 7.5% in a catchment in the United States. In this study, matrix flow and preferential flow were well distinguished according to θ or ψ measured by T-TDR probes. Infiltration processes dominated by matrix flow and preferential flow accounted for 75% (i.e., A1–A3) and 25% (i.e., A4) of observations in the area beneath a tree, respectively. For the study issue 2, therefore, matrix flow and preferential flow underneath a tree can be effectively detected by the T-TDR probes in a short observation period. Although matrix flow dominated the infiltration process in our site's root environment, preferential flow may cause average θ or ψ at all points to reach their maximum values (e.g., at T1 shown in Figure 5). Moreover, tree roots may enhance or interrupt soil water movement. A4 contributed the highest soil water storage and most frequent saturation occurrence during the wetting process among the four measurement lines (Figure 8), but showed the minimum depletion rate during the drying process (Figure 10). This result suggests that the area near the coarse root served as a "hot spot" that exhibited sensitive responses to wetting, whereas rooted-induced preferential flow acted only for a short time. By contrast, the lateral root running parallel to the soil profile at A2 created a "cold spot" underneath the root, where the changes in θ and ψ were small and slow during the both wetting (Figures 5–8) and drying processes (Figures 9 and 10). This indicates that the lateral root somehow interrupted downward movement of the wetting front during the wetting processes, and affected soil water redistribution during drying.

For the study issue 3, we demonstrated that the architecture of roots has important implications for soil water dynamics during both wetting and drying processes, and these effects vary greatly in spatial and temporal terms. Thus, a measurement system with high spatial and temporal resolution is necessary for monitoring preferential flow or irregular patterns of soil water redistribution. Although the performance of the calibrated T-TDR probes was equivalent to EC-5 sensors under both laboratory and field conditions (see Figures S4 and S6), it was hard to evaluate whether soils reached saturated conditions or to describe soil water movements in soil layers based only on a single source of the dataset ψ from the EC-5 sensors (see Figure S7). Information from single source might be able to describe soil water changes under simple laboratory conditions, but information from multiple sources are more desired for monitoring soil water dynamics under heterogeneous field conditions. We suggest that the use of T-TDR probes to measure θ and ψ at the same locations is an effective method to simultaneously evaluate soil water storage and water fluxes in heterogeneous environments with tree roots. Integrated information from multiple sources of θ and ψ could greatly help to improve the accuracy for detecting the presence of preferential flow in a short measurement period without disturbing soil profiles.

5. Conclusions

Although the use of T-TDR probes has been proposed in previous studies, T-TDR probes have not been applied in the field. This study modified the design of the T-TDR probe to enable its use for field measurements. The θ and ψ collected simultaneously by 11 T-TDR probes with high spatial resolution were used to investigate temporal and spatial variations in soil water dynamics beneath a tree in a forest stand. The main results are summarized below.

1. The relationship between the mean and standard deviation of spatial θ and ψ showed convex-upward shapes and negative curvilinear shapes, respectively. High spatial variability was observed at intermediate values of θ and small values of ψ, which indicates the need for θ measurement in wetter conditions and ψ measurement in drier conditions.

2. Infiltration processes dominated by matrix flow and preferential flow accounted for 75% and 25% of observations taken beneath the tree, respectively. Although matrix flow dominated the infiltration process in the root environment, preferential flow could cause the average θ and ψ at all of the locations to reach their maxima.

3. A coarse root served as a "hot spot" that exhibited sensitive responses to wetting, although this root-induced preferential flow acted only for a short time in rainfall events. A "cold spot" existed underneath a lateral root where the hydrological responses were insensitive.

The greatest merit of a T-TDR probe is the simultaneous measurements of θ and ψ at the same point, which can reduce the number of sensors needed for accurate observations. Additionally, it could satisfy the need for effective evaluation of soil water storage, saturated or unsaturated conditions, and soil water movement at a field site containing tree roots. It is hard to evaluate soil water storage or to describe soil water movements in soil layers based only on a single source of θ or ψ. Using several T-TDR probes can capture the characteristics of both θ and ψ, and could help to evaluate soil water dynamics when one exhibited large spatial variation during the wetting or drying processes. Integrated information from multiple sources of θ and ψ could greatly help to improve the accuracy for detecting the presence of preferential flow in a short measurement period without disturbing a soil profile.

References

1. Liang, W.-L.; Kosugi, K.; Mizuyama, T. Characteristics of stemflow for tall stewartia (Stewartia monadelpha) growing on a hillslope. *J. Hydrol.* **2009**, *378*, 168–178. [CrossRef]
2. Keim, R.F.; Skaugset, A.E.; Weiler, M. Temporal persistence of spatial patterns in throughfall. *J. Hydrol.* **2005**, *314*, 263–274. [CrossRef]
3. Levia, D.F.; Germer, S. A review of stemflow generation dynamics and stemflow-environment interactions in forests and shrublands. *Rev. Geophys.* **2015**, *53*, 673–714. [CrossRef]
4. Beven, K.; Germann, P. Macropores and water flow in soils. *Water Resour. Res.* **1982**, *18*, 1311–1325. [CrossRef]
5. Liang, W.-L.; Kosugi, K.; Mizuyama, T. Soil water dynamics around a tree on a hillslope with or without rainwater supplied by stemflow. *Water Resour. Res.* **2011**, *47*, W02541. [CrossRef]
6. Germer, S. Development of near-surface perched water tables during natural and artificial stemflow generation by babassu palms. *J. Hydrol.* **2013**, *507*, 262–272. [CrossRef]
7. Krämer, I.; Hölscher, D. Soil water dynamics along a tree diversity gradient in a deciduous forest in Central Germany. *Ecohydrology* **2010**, *3*, 262–271. [CrossRef]
8. Liang, W.-L.; Kosugi, K.; Mizuyama, T. Soil water redistribution processes around a tree on a hillslope: The effect of stemflow on the drying process. *Ecohydrology* **2015**, *8*, 1381–1395. [CrossRef]

9. Kulli, B.; Stamm, C.; Papritz, A.; Fluhler, H. Discrimination of flow regions on the basis of stained infiltration patterns in soil profiles. *Vadose Zone J.* **2003**, *2*, 338–348. [CrossRef]

10. Noguchi, S.; Tsuboyama, Y.; Sidle, R.C.; Hosoda, I. Morphological characteristics of macropores and the distribution of preferential flow pathways in a forested slope segment. *Soil Sci. Soc. Am. J.* **1999**, *63*, 1413–1423. [CrossRef]

11. Sander, T.; Gerke, H.H. Preferential flow patterns in paddy fields using a dye tracer. *Vadose Zone J.* **2007**, *6*, 105–115. [CrossRef]

12. Lin, H.; Zhou, X. Evidence of subsurface preferential flow using soil hydrologic monitoring in the Shale Hills catchment. *Eur. J. Soil Sci.* **2008**, *59*, 34–49. [CrossRef]

13. Lozano-Parra, J.; van Schaik, N.L.; Schnabel, S.; Gómez-Gutiérrez, Á. Soil moisture dynamics at high temporal resolution in a semiarid Mediterranean watershed with scattered tree cover. *Hydrol. Process.* **2016**, *30*, 1155–1170. [CrossRef]

14. Gwak, Y.; Kim, S. Factors affecting soil moisture spatial variability for a humid forest hillslope. *Hydrol. Process.* **2017**, *31*, 431–445. [CrossRef]

15. Bouten, W.; Schaap, M.G.; Bakker, D.J.; Verstraten, J.M. Modeling soil water dynamics in a forested ecosystem.1. A site specific evaluation. *Hydrol. Process.* **1992**, *6*, 435–444. [CrossRef]

16. Gardenas, A.I.; Simunek, J.; Jarvis, N.; van Genuchten, M.T. Two-dimensional modelling of preferential water flow and pesticide transport from a tile-drained field. *J. Hydrol.* **2006**, *329*, 647–660. [CrossRef]

17. Faybishenko, B. Comparison of laboratory and field methods for determining the quasi-saturated hydraulic conductivity of soils. In Proceedings of the Characterization and Measurement of the Hydraulic Properties of Unsaturated Porous Media, Riverside, CA, USA, 22–24 October 1997; pp. 279–292.

18. Morgan, K.; Parsons, L.; Adair Wheaton, T. Comparison of laboratory- and field-derived soil water retention curves for a fine sand soil using tensiometric, resistance and capacitance methods. *Plant. Soil* **2001**, *234*, 153–157. [CrossRef]

19. Pachepsky, Y.; Rawls, W.J.; Gimenez, D. Comparison of soil water retention at field and laboratory scales. *Soil Sci. Soc. Am. J.* **2001**, *65*, 460–462. [CrossRef]

20. Basile, A.; Ciollaro, G.; Coppola, A. Hysteresis in soil water characteristics as a key to interpreting comparisons of laboratory and field measured hydraulic properties. *Water Resour. Res.* **2003**, *39*, 1355. [CrossRef]

21. Lozano-Parra, J.; Schnabel, S.; Ceballos-Barbancho, A. The role of vegetation covers on soil wetting processes at rainfall event scale in scattered tree woodland of Mediterranean climate. *J. Hydrol.* **2015**, *529*, 951–961. [CrossRef]

22. Metzger, J.C.; Wutzler, T.; Dalla Valle, N.; Filipzik, J.; Grauer, C.; Lehmann, R.; Roggenbuck, M.; Schelhorn, D.; Weckmüller, J.; Küsel, K.; et al. Vegetation impacts soil water content patterns by shaping canopy water fluxes and soil properties. *Hydrol. Process.* **2017**, *31*, 3783–3795. [CrossRef]

23. Ghazavi, G.; Thomas, Z.; Hamon, Y.; Marie, J.C.; Corson, M.; Merot, P. Hedgerow impacts on soil-water transfer due to rainfall interception and root-water uptake. *Hydrol. Process.* **2008**, *22*, 4723–4735. [CrossRef]

24. Leung, A.K.; Garg, A.; Coo, J.L.; Ng, C.W.W.; Hau, B.C.H. Effects of the roots of Cynodon dactylon and Schefflera heptaphylla on water infiltration rate and soil hydraulic conductivity. *Hydrol. Process.* **2015**, *29*, 3342–3354. [CrossRef]

25. Seyfried, M.S.; Wilcox, B.P. Soil water storage and rooting depth: Key factors controlling recharge on rangelands. *Hydrol. Process.* **2006**, *20*, 3261–3275. [CrossRef]

26. Vaz, C.M.P.; Hopmans, J.W.; Macedo, A.; Bassoi, L.H.; Wildenschild, D. Soil water retention measurements using a combined tensiometer-coiled time domain reflectometry probe. *Soil Sci. Soc. Am. J.* **2002**, *66*, 1752–1759. [CrossRef]

27. Vaz, C.M.P.; Hopmans, J.W. Simultaneous measurement of soil penetration resistance and water content with a combined penetrometer–TDR moisture probe. *Soil Sci. Soc. Am. J.* **2001**, *65*, 4–12. [CrossRef]

28. Kosugi, K.; Yamakawa, Y.; Masaoka, N.; Mizuyama, T. A combined penetrometer-moisture probe for surveying soil properties of natural hillslopes. *Vadose Zone J.* **2009**, *8*, 52–63. [CrossRef]

29. Nissen, H.H.; Moldrup, P.; de Jonge, L.W.; Jacobsen, O.H. Time domain reflectometry coil probe measurements of water content during fingered flow. *Soil Sci. Soc. Am. J.* **1999**, *63*, 493–500. [CrossRef]

30. Nissen, H.H.; Moldrup, P.; Henriksen, K. High-resolution time domain reflectometry coil probe for measuring soil water content. *Soil Sci. Soc. Am. J.* **1998**, *62*, 1203–1211. [CrossRef]

31. Katsura, S.; Kosugi, K.; Mizuyama, T. Application of a coil-type TDR probe for measuring the volumetric water content in weathered granitic bedrock. *Hydrol. Process.* **2008**, *22*, 750–763. [CrossRef]

32. Subedi, S.; Kawamoto, K.; Karunarathna, A.K.; Moldrup, P.; Wollesen de Jonge, L.; Komatsu, T. Mini tensiometer-time domain reflectometry coil probe for measuring soil water retention properties. *Soil Sci. Soc. Am. J.* **2013**, *77*, 1517–1528. [CrossRef]

33. Toll, D.G.; Hassan, A.A.; King, J.M.; Asquith, J.D. New devices for water content measurement. In Proceedings of the 18th International Conference on Soil Mechanics and Geotechnical Engineering, Paris, France, 2–6 September 2013; pp. 1199–1202.

34. Lai, Y.-J.; Chang, C.-S.; Tsao, T.-M.; Wey, T.-H.; Chiang, P.-N.; Wang, Y.-N. Preliminary assessment of soil erosion impact during forest restoration process using self-designed tiny weirs. *J. Exp. For. Natl. Taiwan Univ.* **2013**, *27*, 273–284, (In Chinese, with English abstract).

35. Liang, W.-L.; Kosugi, K.; Mizuyama, T. Heterogeneous soil water dynamics around a tree growing on a steep hillslope. *Vadose Zone J.* **2007**, *6*, 879–889. [CrossRef]

36. Penna, D.; Tromp-van Meerveld, H.J.; Gobbi, A.; Borga, M.; Dalla Fontana, G. The influence of soil moisture on threshold runoff generation processes in an alpine headwater catchment. *Hydrol. Earth Syst. Sci.* **2011**, *15*, 689–702. [CrossRef]

37. Campbell. *TDR100 Instruction Manual*; Campbell Scientific Inc.: Logan, UT, USA, 2000.

38. Takagi, K.; Lin, H.S. Temporal dynamics of soil moisture spatial variability in the shale hills critical zone observatory. *Vadose Zone J.* **2011**, *10*, 832–842. [CrossRef]

39. Liang, W.-L.; Li, S.-L.; Hung, F.-X. Analysis of the contributions of topographic, soil, and vegetation features on the spatial distributions of surface soil moisture in a steep natural forested headwater catchment. *Hydrol. Process.* **2017**, *31*, 3796–3809. [CrossRef]

40. Bogena, H.R.; Herbst, M.; Huisman, J.A.; Rosenbaum, U.; Weuthen, A.; Vereecken, H. Potential of wireless sensor networks for measuring soil water content variability. *Vadose Zone J.* **2010**, *9*, 1002. [CrossRef]

41. Penna, D.; Borga, M.; Norbiato, D.; Dalla Fontana, G. Hillslope scale soil moisture variability in a steep alpine terrain. *J. Hydrol.* **2009**, *364*, 311–327. [CrossRef]

42. Rosenbaum, U.; Bogena, H.R.; Herbst, M.; Huisman, J.A.; Peterson, T.J.; Weuthen, A.; Western, A.W.; Vereecken, H. Seasonal and event dynamics of spatial soil moisture patterns at the small catchment scale. *Water Resour. Res.* **2012**, *48*, W10544. [CrossRef]

43. Garcia-Estringana, P.; Latron, J.; Llorens, P.; Gallart, F. Spatial and temporal dynamics of soil moisture in a Mediterranean mountain area (Vallcebre, NE Spain). *Ecohydrology* **2012**, *6*, 741–753. [CrossRef]

44. Western, A.; Grayson, R.; Blöschl, G.; Wilson, D. Spatial variability of soil moisture and its implications for scaling. In *Scaling Methods in Soil Physics*; Pachepsky, Y., Radcliffe, D.E., Selim, H.M., Eds.; CRC Press: Boca Raton, FL, USA, 2003; pp. 119–142.

45. Choi, M.; Jacobs, J.M. Soil moisture variability of root zone profiles within SMEX02 remote sensing footprints. *Adv. Water Resour.* **2007**, *30*, 883–896. [CrossRef]

46. Famiglietti, J.S.; Ryu, D.; Berg, A.A.; Rodell, M.; Jackson, T.J. Field observations of soil moisture variability across scales. *Water Resour. Res.* **2008**, *44*, W01423. [CrossRef]

47. Zucco, G.; Brocca, L.; Moramarco, T.; Morbidelli, R. Influence of land use on soil moisture spatial–temporal variability and monitoring. *J. Hydrol.* **2014**, *516*, 193–199. [CrossRef]

48. Greminger, P.J.; Sud, Y.K.; Nielsen, D.R. Spatial variability of field-measured soil-water characteristics. *Soil Sci. Soc. Am. J.* **1985**, *49*, 1075–1082. [CrossRef]

49. Yeh, T.C.J.; Gelhar, L.W.; Wierenga, P.J. Observations of spatial variability of soil-water pressure in a field soil. *Soil Sci.* **1986**, *142*, 7–12. [CrossRef]

50. Yu, H.; Yang, P.; Lin, H. Spatiotemporal patterns of soil matric potential in the Shale Hills Critical Zone Observatory. *Vadose Zone J.* **2015**, *14*. [CrossRef]

51. Liang, W.-L.; Chan, M.-C. Spatial and temporal variations in the effects of soil depth and topographic wetness index of bedrock topography on subsurface saturation generation in a steep natural forested headwater catchment. *J. Hydrol.* **2017**, *546*, 405–418. [CrossRef]

52. Ghestem, M.; Sidle, R.C.; Stokes, A. The influence of plant root systems on subsurface flow: Implications for slope stability. *BioScience* **2011**, *61*, 869–879. [CrossRef]

53. Yunusa, I.; Mele, P.; Rab, M.; Schefe, C.; Beverly, C. Priming of soil structural and hydrological properties by native woody species, annual crops, and a permanent pasture. *Aust. J. Soil Res.* **2002**, *40*, 207–220. [CrossRef]

54. Weiler, M. Macropores and preferential flow-a love-hate relationship. *Hydrol. Process.* **2017**, *31*, 15–19. [CrossRef]